PROGRESS IN THE HIGH CURRENT EXPERIMENT (HCX) FEBRUARY-JULY 2002[1]

P.A. Seidl[a], D. Baca[a], F.M. Bieniosek[a], B. Bukh[a,b], C.M. Celata[a], A. Coorey[a,c], C. Dugan[a,d], A. Faltens[a], A. Friedman[e], D.P. Grote[e], I. Haber[f], K. Jordan[a,g], J.W. Kwan[a], S.M. Lund[e], E.P. Lee[a], B.G. Logan[a], A.W. Molvik[e], L. Prost[a,g], G. Sabbi[a], W.W. Waldron[a]

(a) Lawrence Berkeley National Laboratory, Berkeley, CA 94720 & The Heavy Ion Fusion Virtual National Laboratory (HIF-VNL)

(b) City College of San Francisco, San Francisco, CA 94112

(c) Univ. of California Los Angeles, Los Angeles, CA 90095

(d) Rensselaer Polytechnic Institute, Troy, NY 12180

(e) Lawrence Livermore National Laboratory, Livermore, CA 94550 & HIF-VNL

(f) Univ. of Maryland, College Park, MD 20742

(g) Univ. of California Berkeley, Berkeley, CA 94720

Abstract

This paper reports progress in the HCX experimental program since the last HIF-VNL Program Advisory Committee Review (February 14-15 2002). On July 25 2002 the experiment was shut down for about four weeks to move the control room.

A principal area of effort has been to obtain and evaluate the first experimental results carried out with a matched and well-aligned K^+ ion beam transported through 10 electrostatic transport quadrupoles. These are the main results and highlights to date:

A1. There is no emittance growth within the sensitivity of the diagnostics, and little beam loss. The beam centroid is aligned to within 0.5 mm and 2 mrad of the central axis of the channel, and the envelope mismatch amplitude is <2 mm.

A2. A long-life, alumino-silicate source has replaced a contact-ionization source, eliminating depletion-induced experimental uncertainties.

A3. Significant differences between the experimental data and early theoretical calculations of the beam envelope propagating through the electrostatic quadrupoles were encountered. More detailed envelope models and simulations were developed and experimental parameter sensitivities were analyzed. This work has resolved most of the discrepancy and achievable limits on envelope predictability and control are being probed.

A4. The experimental current density distribution, J(x,y), and phase-space data are being used to initialize high-resolution simulations to enable realistic modeling and detailed comparisons to experiment.

In other areas of HCX R&D:

B1. We have made progress in the development of new time-resolved phase-space diagnostics that will speed up data acquisition in this and other upcoming beam experiments in the HIF-VNL.

B2. Preliminary results from a Gas, Electron Source Diagnostic (GESD) are presented, which measures gas desorption and secondary electrons. The secondary emission yield varies as $\cos^{-1}(\square)$, as predicted theoretically. Data from the GESD will be relevant to upcoming experiments on particle loss and electron effects in a magnetic quadrupole lattice.

B3. The design of the superconducting quadrupole cryostat needed for a future phase of HCX experimentation has been refined and a vendor has been selected from a group of five that submitted bids. Construction of an optimized prototype quadrupole began this summer.

B4. The design of a longitudinal bunch control induction module is near a final design review (DOE SBIR Phase II). The module will apply agile control of the acceleration waveforms to correct for space charge field effects on the head/tail of the beam.

1. INTRODUCTION

The High Current Experiment (HCX) located at Lawrence Berkeley National Lab and carried out by the HIF-VNL is designed to explore the physics of intense

[1] Supported by the Office of Energy Research, US DOE, at LBNL and LLNL under contract numbers DE-AC03-76SF00098, W-7405-Eng-48.

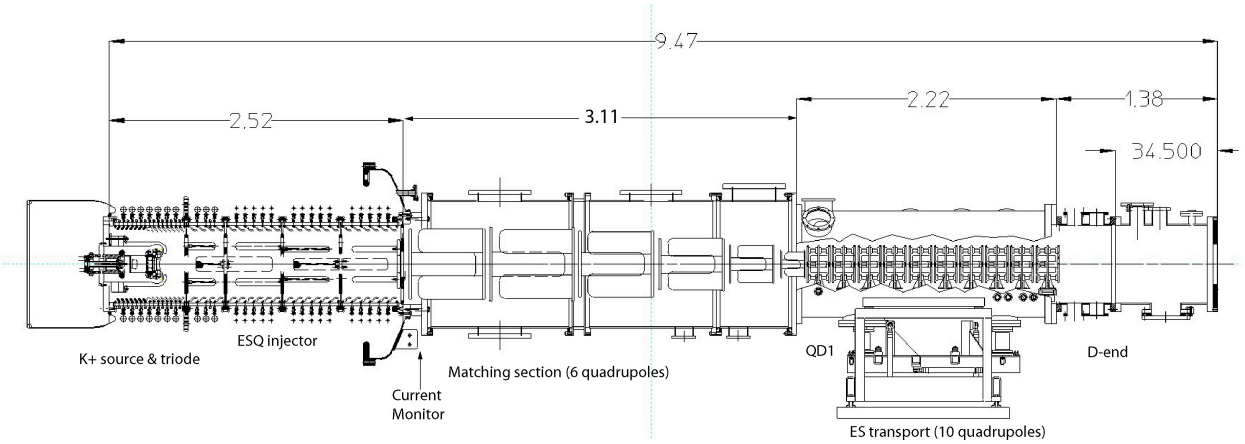

Figure 1: Initial experimental configuration. The secondary electron, ion and gas diagnostic was installed downstream of the end station (D-end) diagnostic.

beams with line-charge density of about 0.2 μC/m and pulse duration 4<τ<10 μs, close to the values of interest for a fusion driver [1]. Experiments are performed near driver injection energy (1-1.8 MeV). HCX beam transport is at present mainly based on electrostatic quadrupole focusing, which provides the most efficient option at low energy and provide clearing fields which sweep out unwanted electrons. However, magnetic transport experiments will also be performed to gain operational experience and to explore special limitations associated with magnetic focusing, in particular the onset of transport-limiting effects due to electrons trapped in the potential well of the ion beam.

2. EXPERIMENTAL CONFIGURATION

The present configuration begins with the K^+ ion source and injector, an electrostatic quadrupole matching section (six quadrupoles), and the first 10 electrostatic transport quadrupoles. An additional 20-30 electrostatic quadrupoles to be added to the experiment are planned for FY03, which would increase the transport length to 4.5-6•(2πv/ω$_p$) plasma periods. Theoretical models predict that this would be just enough to observe the relaxation of phase space and distribution inhomogeneities.

At the end of the beam line is a multi-purpose diagnostic station (D-end). Beam diagnostics are also located at the interface of the matching section and the ten transport quadrupoles. The present layout of the apparatus is shown in Fig. 1. The diagnostics at the first transport quadrupole in the periodic lattice (QD1) are transverse slit scanners and kapton film that measure phase space projections, and a Faraday cup which measures total beam current. The Gas and Electron Source Diagnostic (GESD) is located at the end of D-end.

All commissioning and preliminary measurements have been made at 1.0 MeV, to avoid any high voltage insulation issues in the injector. The beam energy at present is limited to 1.5 MeV until the water resistor that distributes the voltage along the injector column is modified. To date, contact-ionization and alumino-silicate ion sources have been used, as described in [2]. The injector beam characterization measurements and the very first measurements through the HCX were made using the contact ionization source, before switching to the alumino-silicate source (~100 mm diameter) in April 2002. Earlier versions of alumino-silicate sources suffered from poor current-density uniformity. There was a considerable alumino-silicate large-source R&D effort during FY01-2 aimed at improving the uniformity. The newest alumino-silicate source produces profiles similar to the contact ionization source, and transverse phase space distributions and envelope parameters at QD1 (within experimental reproducibility checks, Sec. 3) also comparable to those of the contact-ionization source. The alumino-silicate source has a much longer lifetime, which has increased the beam availability for experiments and diminished uncertainties from depletion-related beam current variations. Furthermore, the contact ionization source was removed from the system for replenishing after depletion (every 1-2 weeks), which caused alignment changes from removal and installation. The emission uniformity of a duplicate alumino-silicate source will be measured in detail at the STS500 as part of the HIF-VNL source and injector research agenda. (This does not indicate a narrowing of source options for HIF; contact ionization sources are still viable options, because in-situ replenishment concepts have been used previously [3] and are ready for further development when the need arises.)

First beam was transported in the HCX on January 11, 2002, less that one month after the assembly of the initial configuration. The experiment was interrupted (since July 25) for approximately one month to move the control room to a seismically safe area.

The work presented in this paper substantially meets the Fusion Energy Sciences Program Execution Agreement target milestone (9/30/02) to make a preliminary determination of limits on allowable beam current for a driver scale beam near injection.

3. MATCHING & TRANSPORT THROUGH THE FIRST 10 ES QUADRUPOLES

The six-quadrupole matching section is designed to compress the beam area transversely by a factor ≈25 and produce the matched beam parameters for periodic transport in the electrostatic lattice. In this significant beam manipulation the radii of the first (QM1) and last (QM6) matching quadrupole bores are r_p=100 mm and 31 mm respectively, and the maximum envelope excursions occur in the first and second quadrupoles, with the beam filling radii up to 0.8• r_p. The beam centroid exiting the injector is offset from the beam line axis by a few millimeters and milliradians, and the centroid undergoes betatron oscillations through the first three (QM1-3) quadrupoles of the matching section until being corrected in QM4-6. QM4-6 may each be displaced in the horizontal and vertical directions by ±15mm to correct the beam centroid offset. Typical matching (QM1-6) and transport quadrupole (Q1-10) voltages and displacements are indicated in Table 1. (Experiments at higher injection energy will require proportional increase in the quadrupole potentials to achieve a nearly identical envelope solution.)

Although the beam fills a relatively large fraction of the aperture in the early part of the matching section, pickup signals capacitively coupled to the quadrupole electrodes indicate beam loss is less than 0.5% through the middle, or "flattop" of the beam pulse. Beam loss at the head and tail of the current pulse may be greater, and is presently being studied. The pickup signal due to lost ions is effectively amplified by the large (>10) secondary electron coefficient, making this diagnostic more sensitive to beam loss than comparisons of the current transformer at the injector exit to the Faraday cup at QD1. The Faraday cup-current transformer ratio is >95%, where the relative accuracy of this measurement is a few percent.

Quad ID	V_Q	Gradient	Aperture radius	□x	□y
	(kV)	(kV/cm^2)	(mm)	(mm)	(mm)
QM1	±42.8	.86	10	0	0
QM2	±32.8	.81	9	0	0
QM3	±35.98	1.0	8.5	0	0
QM4	±28.56	1.3	6.7	+0.4	+0.8
QM5	±36.15	3.0	4.9	-3.9	+1.3
QM6	±41.84	8.7	3.1	-2.0	-3.9
Q1-10	±25.5	9.6	2.3	0	0

Table 1: Typical matching section voltages and steering quadrupole offsets for operation at E_{beam} = 1.0 MeV.

The steering quadrupole displacements are determined by calculating the (single particle) trajectory through QM4-6 for a misaligned beam, and then solving for the required displacements. Three steering quadrupoles QM4-6) are used to align the beam centroid at QD1 (instead of the minimum of two displacements) subject to the additional constraint of minimizing the sum of displacements of the lenses. Following such a procedure, the beam centroid positions (<x>, <y>) and angles (<x'>, <y'>) are routinely within 0.5 mm and 2 mrad of the central axis of the channel. (The uncorrected centroid offset of the beam is several mm and mrad at QD1. This is mainly due to the beam centroid offset at the entrance to the matching section resulting from imperfect source alignment.)

The phase space measurements at QD1 are shown in Fig. 2, along with the calculated envelope excursions downstream. The near-linear phase space correlation is due to the alternating gradient focusing. A perfect beam

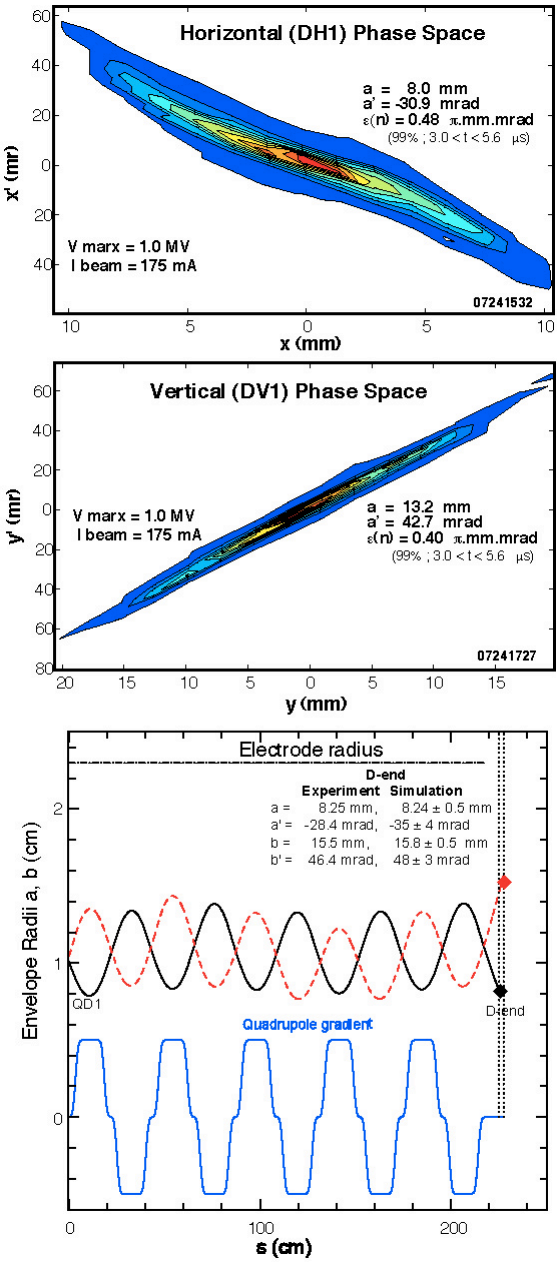

Figure 2: Measured QD1 phase space and the calculated envelope to D-end are compared to D-end envelope data (diamonds). The tabulated envelope uncertainty at D-end are 1□ of a Monte Carlo set, from uniformly distributed (±0.5mm, ±1 mrad) measurement uncertainties at D1.

would have an elliptical distribution. The stability and reproducibility of the envelope measurements has been characterized by a standard deviation of ≈0.3 mm and ≈1 mrad among five repeated measurements. For the best data sets, the mismatch amplitude is ≈1 mm about the ideal, periodic matched beam envelope. The achievable beam envelope and centroid control are key ingredients in determining the allowable filling factor without significant beam loss and emittance growth. Presently, the envelope fills ≈60% of the available bore diameter in the transport channel.

The calculated envelope is in agreement with the data at D-end to within 0.3 mm and 7 mrad. Early calculations of the envelope showed a much larger discrepancy, which led to an analysis of several effects, which collectively explained most of the disagreement. The effects are:

1. Realistic fringe field model based on 3D field calculations.
2. Quadrupole E_z and corresponding radial focusing force.
3. Corrections for the grounded slit plates of the intercepting diagnostics that short out the self-field of the beam near the diagnostic.
4. More thorough crosschecks on the beam current and energy.
5. Allowance for the uncertainty in the experimental measurements as characterized by the reproducibility studies.

The improvements will make the envelope model an accurate theoretical and experimental beam control tool (instantaneous turn around) for this and future VNL experiments.

Within the experimental sensitivity there is no evidence of emittance growth at D-end. Four phase space measurements, each with slightly different matching section solutions but the same settings for Q1-10, show a 1□ spread of □□/□≈ 3% at QD1, and 8% at D-end. Systematic biases such as those due to finite slit widths and rotational misalignments, are still being analyzed, and may contribute an error of 10-20%.

In the context of multiple beam arrays for heavy-ion fusion, electrostatic quadrupoles composed of cylindrical electrodes makes a compact unit cell. For the beam measurements to date, the current density averaged over a unit cell is ≈40 A/m^2 (denominator includes the area occupied by the beam focusing electrodes between adjacent channels of an array), and future measurements at 1.8 MeV will increase this by 2-3x. Furthermore, it appears from these measurements that higher filling factors should be possible. Simulations predict that 80% of the aperture radius may be possible, with negligible beam degradation [4]. Compiling data to determine the optimum filling factor is a principal goal the experiment.

4. BEAM CHARGE DISTRIBUTION

We observe a diamond-shaped beam pattern at QD1 (Fig. 3) and at D-end, which is attributed to nonlinear fields (that is, anharmonic field components not varying in direct proportion to the transverse coordinates) in the ESQ injector and from the electrostatic image in the matching section. PIC simulations indicate that the predicted emittance growth for a similar distribution through 50 lattice periods (close to IBX length [5]) is very small for beam filling factors <80%.

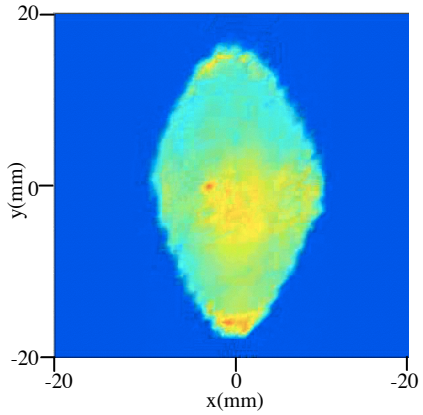

Figure 3: Beam current density profile J(x,y, t≈midpulse) measured with crossed slits at QD1.

The time-resolved crossed-slit data show that at QD1 the profile of the beam during the rise and fall of the beam current pulse (Fig. 4) is larger than during the flattop. Ballooning of the beam head was predicted for the beam exiting the injector from 3D particle-in-cell simulations and is attributed to a mismatch of current and energy. Calculations of the head-tail dynamics through the rest of the HCX are underway.

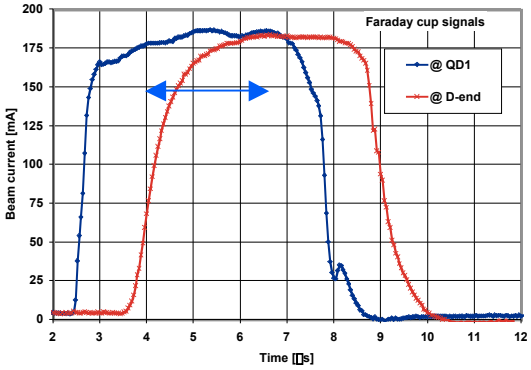

Figure 4: Beam current pulse from Faraday cups at QD1 and D-end. The data in Figs. 2 and 3 are from the relatively flat interval between the rise and fall of the beam pulse (red arrow), presently ≈2.5 □sec.

5. DIAGNOSTICS DEVELOPMENT

Kapton film has been used to provide high-resolution images of the beam profile at (Fig. 5) QD1 and D-end.

With the high intensity beam (≈0.6mA/mm^2 compared to <0.05 mA/mm^2 for earlier scaled experiments [6]),

calibration checks indicated that the response is nearly linear and the exposures are not saturated [7]. All the J(x,y) data will be used with the phase space data at QD1 to construct a consistent particle distribution for simulation studies. We are investigating the utility of optical diagnostics for rapid and highly detailed measurements of beam phase space distributions.

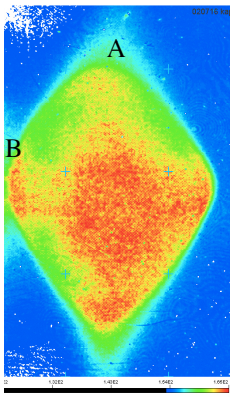

Figure 5: J(x,y) of the beam from kapton film exposed to ≈ 40 beam pulses at QD1. Time-resolved crossed-slit data shows that the faint signal at the top (A) and bottom (compared to Fig. 3) is due to head & tail variations. The enhancement (B) at the left is due to proximity of independent slit measurements on the same support paddle.

Figure 6 shows a composite image of a typical slit scan from a prototype optical emittance scanner. The beam is imaged through the existing slits, already utilized in the conventional emittance scanner (Fig. 2), onto a thin alumina ceramic wafer, where charge buildup is prevented by secondary electron emission from a grounded wire grid placed directly on the screen.

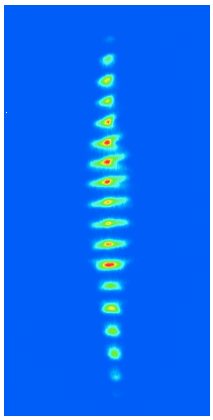

Figure 6: Composite series of false-color images of the beam at D-end in a vertical slit scan with spacing of slit locations of 0.56 mm. The slit width is 0.05 mm. The beam is elongated at this location because of the vertical divergence and horizontal convergence of the beam under the conditions of the measurement. The imaged area shown is 2 cm x 6 cm.

Alumina fluoresces efficiently with an emission peak at about 350 nm (in the near-UV) and has adequate lifetime and fluorescence decay time. (The response time of the alumina is shorter than the rise (200 ns) and fall time of the beam current pulse.) The images are viewed behind the wafer with a gated, image-intensified CCD camera. Each image shown in Figure 6 represents the open-shutter optical image on the ceramic wafer from a single beam pulse. The slit is oriented horizontally and is moved vertically by a constant 0.56 mm from pulse to pulse. The images can be integrated to provide a simulated slit scan for comparison with conventional slit scanner data. In addition, a large amount of new phase space correlation information is available from the shapes of the images. Detailed analysis of the data is underway. In the future the slits may be replaced with a pepper-pot hole arrangement, which would provide fully correlated four-dimensional transverse phase space.

6. MEASUREMENTS OF SECONDARY ELECTRONS AND ATOMS

The Gas-Electron Source Diagnostic (GESD) is designed to measure the gas desorption and secondary electron and ion emission from heavy-ion beams impacting a surface (Fig. 7). Approximately 0.1% of the beam current passing through a small aperture strikes a target, adjustable between angles of incidence from 75° to 88° relative to normal.

We observed a significant change in secondary emission with the angle of the target (Fig. 8). The data is shown for grid biases of +50, 100, and 150 V with the target biased to –40 V. The relative insensitivity of the current to the range of bias voltage shows excellent saturation, indicating a reliable measurement of the secondary electron current. The secondary emission coefficient varies from ~40 to ~185 at the 150 V grid bias. Beam ions lost to the walls will be near grazing incidence, and therefore will have the higher values of secondary emission coefficients.

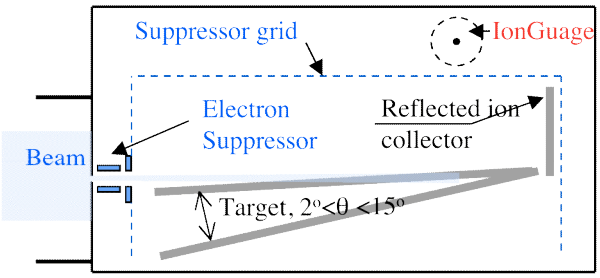

Figure 7: Gas and Electron Source Diagnostic.

These coefficients are preliminary; data with the target biased positive has not provided convincing measurements of the beam current with all secondary electrons suppressed. However, we have estimated the beam current into the GESD from the total beam current (175 mA), the angles of beam expansion, the distance to

the GESD, and the entrance aperture area, to be ~0.14 mA (+100%/-50%).

A beam line of four pulsed magnetic quadrupoles, instrumented with diagnostics to measure the production and energy of trapped electrons, secondary atoms and ions is being assembled [8]. They will be installed downstream of the first group of 10 electrostatic quads in September 2002.

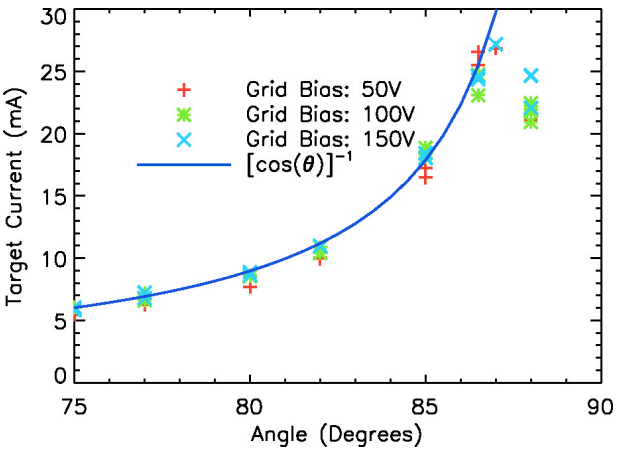

Figure 8: Angular distribution of the secondary electrons measured in the GESD. The target current is measured as a function of the angle of the beam normal to the target. The bias voltages are target = -40 V, catcher = -25 V, and the grid as listed.

7. SUPERCONDUCTING MAGNETS

The design of the cryostat has been refined and a vendor has been selected from a group of five that submitted bids (Fig. 9). The unit contains two quadrupole magnets (an FD doublet) mounted on an alignment tube, the 4 K cold mass container, LN thermal shields and radiation shields, a vacuum vessel and a shielded straight chimney enclosing a pair of Nb_3Sn bus bars connected to the coil leads. The chimney is needed to maximize the space available for induction acceleration cores surrounding the transport line. A transition box at the top of the chimney provides interconnection between the quadrupole cryostat and an upper cryostat housing a pair of 3 kA vapor cooled leads (VCL), transfer lines and diagnostics connections.

Construction of an optimized prototype quadrupole began this summer. It is expected to achieve significant improvements in integrated gradient, field quality, coil mechanical support and cost with respect to the first prototype series [9]. The coil ends have been modified, resulting in a longer magnetic length for the same coil length, and better end field quality. In addition, independent optimization of the field quality in the body and ends results in a more efficient cross-section. These combined advantages lead to a 20% increase of the integrated gradient for the same conductor properties.

HCX-type magnets are considered for most of the IBX accelerator in pre-conceptual designs [10]. For some IBX accelerator designs, the magnet requirements for the accelerator can be met by a modified HCX design using a single layer of coils, with significant cost saving potential.

The design of a prototype quadrupole array has started at Advanced Magnet Lab with funding from a DOE SBIR Phase I grant. The main technical objectives are the comparison of different coil layouts, the design of edge coils to both terminate the flux and adjust the field quality, the development of a suitable mechanical design and quench protection scheme, and the design of a cryostat compatible with induction acceleration. Four channels will be used in the first prototype, consistent with the possibility of an IBX upgrade to four beams.

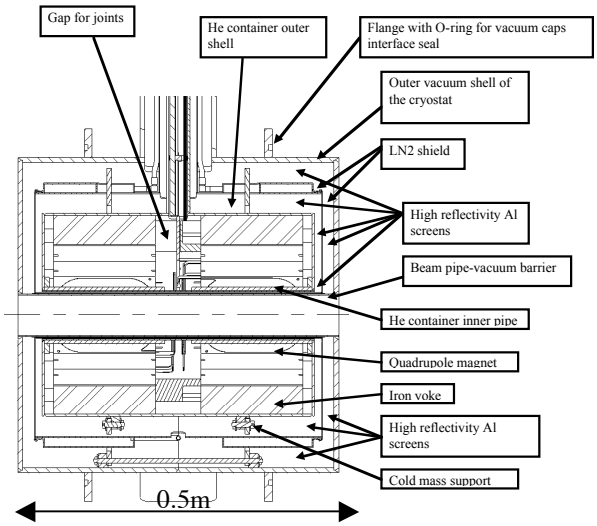

Figure 9: The cryostat for two superconducting quadrupoles is compact to allow room for induction acceleration modules and beam diagnostics.

8. LONGITUDINAL BEAM CONTROL

In the area of longitudinal beam dynamics and control, an induction module is being built by First Point Scientific [11] from a DOE SBIR Phase II grant. The module will apply agile control of the acceleration waveforms to correct for space charge field effects on the head and tail of the beam. The apparatus includes three electrostatic quadrupoles, and a complete system of induction cores and modulators for installation in the HCX lattice between the matching section and the QD1 quadrupole. "Ear" waveforms (± 200kV, actively regulated to ±3%) will prevent the bunch ends from eroding due to the longitudinal self-field of the beam. This module will also regulate 20kV variations during the flattop (to ±0.1%Vinjector) to study consequences of pulse energy variations and correct waveform imperfections. Since February 2002, the design of the module and the three electrostatic quadrupoles required on the inner diameter of

the cores is nearly finalized, and a final design review is planned for September 2002.

9. SUMMARY

The transport results through the first ten electrostatic quadrupoles show good beam control, agreement with an improved envelope model and indicate that transport at larger beam filling factors should be possible with acceptable emittance growth and beam loss. Details of the measured phase space distribution are being used to initialize particle in cell simulations and comparison with theoretical models.

Prototype diagnostic tests show that higher data acquisition rates and sensitivity to more correlations between the transverse phase space measurements will enhance future experimental output. New measurements of secondary electrons, ions and atoms will couple tightly to transport experiments in magnetic quadrupoles.

ACKNOWLEDGMENTS

We are grateful for the excellent technical support from R. Hipple, W. Strelo and their staff.

B. Bukh and A. Coorey were supported in part through the Department of Energy's Community College Initiative in Biotechnology, Environmental Science, and Computing.

C. Dugan was supported in part through the U.S. Department of Energy's Energy Research Undergraduate Laboratory Fellowship program.

REFERENCES

[1] P.A. Seidl, et al. Overview of the Scientific Objectives of the High Current Experiment for Heavy-Ion Fusion Proc. 2001 Part. Accel. Conf. pp. 2932-2934, IEEE #01CH37268C. Piscataway, NJ 08855.

[2] J.W. Kwan et al, "A 1.8 MeV K^+ Injector for the High Current Beam Transport Experiment", Proceedings of the 14th International Symposium on Heavy Ion Inertial Fusion, Moscow, May 26-31, 2002. To be published in LASER AND PARTICLE BEAMS 20 (4), 2002. LBNL-50221.

[3] S. Abbott et al., "Large Aperture Contact Ionized Cs+1 Ion Source for an Induction Linac", IEEE Trans. Nucl. Sci., NS-26 #3 (1979) 3095.

[4] C.M. Celata et al., "Particle-in-Cell Simulations of the Dynamic Aperture of the HCX", Proceedings of the 14th International Symposium on Heavy Ion Inertial Fusion, Moscow, May 26-31, 2002. To be published in LASER AND PARTICLE BEAMS 20 (4), 2002.

[5] J. Barnard et al., "Integrated Experiments for Heavy Ion Fusion: IBX and IRE", Proceedings of the 14th International Symposium on Heavy Ion Inertial Fusion, Moscow, May 26-31, 2002. To be published in LASER AND PARTICLE BEAMS 20 (4), 2002.

[6] W.M. Fawley et al., "Beam dynamics studies with the heavy-ion linear induction accelerator MBE-4", Phys. Plasmas, **4**(3) p. 880 (1997).

[7] F. M. Bieniosek, et al., "Imaging of heavy-ion beams on kapton film", Rev. Sci. Inst., V 73 (8) August, 2002. LBNL-49605.

[8] A.W. Molvik et al., "Electron Effects in Intense, Ion Beam Linacs – Theory and Expermental Planning for HCX", Proceedings of the 14th International Symposium on Heavy Ion Inertial Fusion, Moscow, May 26-31, 2002. To be published in LASER AND PARTICLE BEAMS 20 (4), 2002. LBNL-51009.

[9] A. Faltens et al., "Development of Superconducting Magnets for Heavy Ion Fusion", Proceedings of the 14th International Symposium on Heavy Ion Inertial Fusion, Moscow, May 26-31, 2002. To be published in LASER AND PARTICLE BEAMS 20 (4), 2002. LBNL-50869.

[10] E. Lee, et al., "IBX Rough Design," Proceedings of the HIF-VNL IBX Workshop, October 9-10, 2001, pp. 166. J. Barnard et al., "IBX Straw Person Design," Proceedings of the HIF-VNL IBX Workshop, October 9-10, 2001, pp. 191.

[11] C. Burkhart, "The Closed-loop Amplifier Regulated Driver, a High Accuracy, Low Cost Modulator for HIF Accelerators," US Dept. of Energy SBIR final Report, DE-FG03-00ER83010, May 2001.

APPENDIX

Diagnostic station	QD1	D-end
ε_x [$\pm\ \varepsilon_x(1\sigma)$] (mm•mrad)	63 [±2]	60 [±3]
ε_y [$\pm\ \varepsilon_y(1\sigma)$] (mm•mrad)	54 [±1]	65 [±5]
($\varepsilon_x + \varepsilon_y$)/2 (mm•mrad)	58.5	62.5

Table A1: Horizontal and vertical emittance (un-normalized) averaged over 4 matching solution data sets.

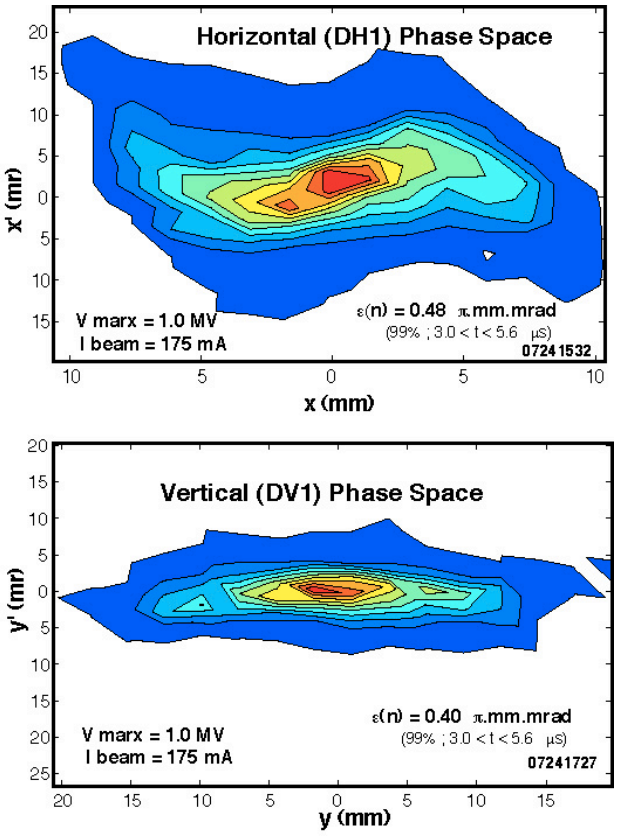

Figure A1: Horizontal and vertical phase space at QD1, with the coherent envelope convergence and divergence removed show more details of the distribution, including the manifestation of focusing imperfections.